Stress release and source scaling of the 2010-2011 Canterbury, New Zealand, earthquake sequence from spectral inversion of ground motion data

Adrien Oth[1] and Anna E. Kaiser[2]

1) European Center for Geodynamics and Seismology, 19, rue Josy Welter, L-7256 Walferdange, Grand-Duchy of Luxembourg, Email: adrien.oth@ecgs.lu

2) GNS Science, 1 Fairway Drive, Avalon 5010, PO Box 30-368, Lower Hutt, New Zealand, Email: a.kaiser@gns.cri.nz

ABSTRACT

The Canterbury earthquake sequence beginning with the 2010 M_W 7.2 Darfield earthquake is one of the most notable and well-recorded crustal earthquake sequences in a low-strain-rate region worldwide and as such provides a unique opportunity to better understand earthquake source physics and ground motion generation in such a tectonic setting. Ground motions during this sequence ranged up to extreme values of 2.2g, recorded during the February 2011 M_W 6.2 event beneath the city of Christchurch. A better understanding of the seismic source signature of this sequence, in particular the stress release and its scaling with earthquake size, is crucial for future ground motion prediction and hazard assessment in Canterbury, but also of high interest for other low-to-moderate seismicity regions where high-quality records of large earthquakes are lacking.

Here we present a source parameter study of more than 200 events of the Canterbury sequence, covering the magnitude range M_W 3 − 7.2. Source spectra were derived using a generalized spectral inversion technique and found to be well characterized by the ω^{-2} source model. We find that stress drops range between 1 and 20 MPa with a median value of 5 MPa, which is a factor of 5 larger than the median stress drop previously estimated with the same method for crustal earthquakes in seismically much more active Japan. Stress drop scaling with earthquake size is nearly self-similar, and we identify lateral variations throughout Canterbury, in particular high stress drops at the fault edges of the two major events, the M_W 7.2 Darfield and M_W 6.2 Christchurch earthquakes.

1. INTRODUCTION

On 4 September 2010, the M_W 7.2 Darfield earthquake struck the Canterbury region on the South Island of New Zealand, giving rise to the beginning of the remarkable Canterbury earthquake sequence (Bannister and Gledhill, 2012). The Darfield event occurred on the previously unmapped Greendale Fault in the Canterbury Plains (Quigley et al., 2010), an area of comparatively low seismicity prior to this event. The area is located ~100 km from the major plate boundary through the South Island (Alpine Fault; Figure 1) and deformation rates over the ~120 km wide Canterbury Plains region are estimated to be ~2mm/yr based on GPS-derived strain rates (Wallace et al. 2007). For these reasons, the source region of this sequence can be viewed as an intra-plate tectonic setting.

On 22 February 2011, the Darfield event was followed by a devastating aftershock of moment magnitude M_W 6.2, located almost immediately below the city of Christchurch, and two further events nearby on 13 June 2011 (M_W 6.0) and 23 December 2011 (M_W 5.9). In particular the former event entailed tragic consequences, claiming 185 lives and causing large-scale destruction throughout the city, with over 9 billion US$ in damage (Bannister and Gledhill, 2012).

The Canterbury earthquakes have produced remarkably intense ground shaking (Fry et al., 2011) and liquefaction phenomena have been widespread throughout the region (Orense et al., 2011; Kaiser et al., 2012). During the M_W 6.2 Christchurch event, ground motions of up to 2.2g (vertical, 1.7g on the horizontal components) were recorded close to the epicenter (Kaiser et al., 2012), and the records of this event are characterized by a very rich high frequency content evident on the vertical component of recordings and at near-source rock site LPCC. Clearly site response phenomena play an important role in the generation of strong ground motion (e.g., Fry et al., 2011; Bradley, 2012). However, previous studies

came to the conclusion that these features observed for the largest Canterbury events are also linked to particularly strong seismic energy radiation relative to their seismic moment, and thus high apparent stress (Fry and Gerstenberger, 2011; Holden, 2011).

The Canterbury earthquake sequence provides a unique opportunity to learn more about the source characteristics of major earthquakes in intra-plate tectonic settings, where events such as the September 2010 Darfield or February 2011 Christchurch earthquakes represent extreme events with very low probability of occurrence. As a consequence, very few high-quality near-source recordings of such events exist worldwide, and as Fry and Gerstenberger (2011) point out, it may well be the case that such extreme ground motions could be a common feature for these types of events. In this context, the source characteristics of the large magnitude events are clearly of interest, but in particular also the scaling of these parameters between small and large events. Up-scaling techniques using recordings of small earthquakes as empirical Green's functions (e.g., Irikura, 1986) are a key element in deterministic seismic hazard assessment in regions where only very limited data from past large magnitude events are available.

The aim of this study is therefore to make use of the rich database of strong motion recordings within the New Zealand GeoNet monitoring network (Petersen et al., 2011) in order to provide an in-depth analysis of the source spectral characteristics of the Canterbury earthquakes. To this end, we use a spectral inversion technique that allows for a separation of source, path and site contributions within the recorded ground motion spectra, and focus on the source term in this article. We first provide a brief overview of the dataset and the methods used, followed by a discussion of the source spectra resulting from the inversion and the calculated stress drops, with particular emphasis on their scaling behavior and lateral variations.

2. DATASET AND SPECTRA CALCULATION

The dataset under investigation consists of 2415 accelerograms from 205 earthquakes that were recorded at 64 stations throughout the Canterbury Plains, with a particular density of recording sites in the Christchurch urban area (Figure 1). Of these 64 stations, 5 belong to the New Zealand National Seismograph Network (NZNSN, Petersen et al., 2011), where broadband and strong-motion instruments are collocated. Strong motion data are acquired with Kinemetrics episensors and 24-bit Quanterra Q330/Q4120 data loggers, sampled at 100 Hz. The remaining stations are part of the New Zealand National Strong Motion Network and are equipped either with Kinemetrics episensors or Canterbury Seismic Instruments (CSI) CUSP units, coupled with 24-bit Quanterra Q330/Q4120 or Kinemetrics Basalt data loggers, most of these providing acceleration records with 18-bit resolution. The sampling rate at the strong motion stations is 200 Hz, and the full recording range is +/- 4g. Detailed information on the seismic networks in New Zealand can be found on the GeoNet website (www.geonet.org.nz).

All records are sourced from the GeoNet strong motion catalogue (ftp://ftp.geonet.org.nz/strong/) and have signal-to-noise ratio larger than 3 in the frequency band of analysis, 0.5 – 20 Hz. During the data selection process, only stations and earthquakes with at least three recordings were considered, and records with peak ground accelerations higher than 0.15g were excluded in order to avoid bias in the source spectra due to the presence of strong non-linear site effects (the applied spectral inversion scheme is based on the assumption of linear soil response and the occurrence of widespread liquefaction clearly indicates the existence of non-linear soil behavior). While seismic moments for all events except the largest ones are determined through the analysis (see following section), it is desirable to have access to independent, robust magnitude estimates

serving as benchmarks. For this purpose, where available, we utilize moment magnitude (M_W) derived from GeoNet regional moment tensor analysis (Ristau, 2008). For the remaining events where only GeoNet local magnitudes (M_L) (e.g., Haines, 1981) are available, we estimate M_W based on these values. In New Zealand M_L has been observed to be systematically biased upwards with respect to M_W (Ristau 2013). To account for this, we adjusted the M_L estimates using the following empirical relationship derived for Canterbury earthquakes: $M_W = M_L - 0.34$ (J. Ristau, personal communication). These magnitude values (hereinafter referred to $M_{W,GeoNet}$) serve as a benchmark for crosschecking the moment magnitudes derived from the spectral fitting procedure detailed below.

Figure 2 shows the distribution of data points in terms of magnitude with respect to hypocentral distance and focal depth. The M_W-distance coverage is excellent with very large numbers of ray path crossings in the source region of the Canterbury earthquake sequence, thereby fulfilling the fundamental prerequisites for the application of the non-parametric spectral inversion scheme outlined below. Most events have focal depths ranging between 5 and 12 km.

For the spectral analysis, we calculated the Fourier amplitude spectra of horizontal component S-wave windows starting 0.5 second before the S-wave onset and ending when 80% of record's energy has been reached (Oth et al., 2011), with a 5% cosine taper applied to the selected windows and a minimum duration of 5 sec in order to ensure enough spectral resolution at lowest frequencies. With this approach, the vast majority of records have window lengths between 5 and 10 sec. For the M_W 7.2 Darfield earthquake that involved complex rupture on multiple fault planes (Beavan et al. 2012), we allowed for a maximum window length of 20 sec, as a compromise between ensuring the inclusion of the entire S-wave window while avoiding too much contamination by surface waves. The

obtained spectra were smoothed around 40 frequency points equidistant on log scale between 0.5 and 20 Hz using the Konno and Ohmachi (1998) windowing function with b=30 and combined into their root-mean-square average. Two examples for this data processing procedure are shown in Figure 3.

3. SPECTRAL INVERSION APPROACH

In order to isolate the earthquake source spectra from the observed S-wave amplitude spectra, we follow the one-step non-parametric generalized inversion technique as outlined by Oth et al. (2011). We only provide a brief summary of the method here and refer the reader to the above-mentioned article and the references therein for further details.

Under the assumption of a convolutional ground motion model, the amplitude spectrum of earthquake ground motions can be written as:

$$U_{ij}(f, M_i, R_{ij}) = S_i(f, M_i) \cdot A(f, R_{ij}) \cdot G_j(f), \tag{1}$$

where $U_{ij}(f, M_i, R_{ij})$ represents the observed spectral amplitude at frequency f (in our case acceleration) obtained at the jth station resulting from the ith earthquake with magnitude M_i, R_{ij} is the hypocentral distance, $S_i(f, M_i)$ represents the source spectrum of the ith earthquake, $A(f, R_{ij})$ accounts for the path effects and $G_j(f)$ is the site response function of the jth station (assuming here that the instrument response is corrected). We linearize equation (1) by taking the logarithm:

$$\log_{10} U_{ij}(f, M_i, R_{ij}) = \log_{10} S_i(f, M_i) + \log_{10} A(f, R_{ij}) + \log_{10} G_j(f), \tag{2}$$

and obtain this way a linear system of the form $\mathbf{Ax} = \mathbf{b}$, which can be solved using appropriate algorithms (e.g., Menke, 1989).

If, as in the present case, a dataset with good distance coverage is available, a non-parametric inversion approach can be used rather than pre-defining a functional form for $A(f, R_{ij})$. In this case, the non-parametric function $A(f, R_{ij})$ implicitly includes all attenuation effects along the travel path (geometrical spreading, anelastic and scattering attenuation, refracted arrivals etc.) in a 1D model, and based on the idea that these properties vary slowly with distance, $A(f, R_{ij})$ is only constrained to be a smooth function of distance (see for instance Castro et al., 1990, for the implementation of this condition) and to take the value $A(f, R_0) = 1$ at some reference distance R_0, which is set to 5 km in this work.

Finally, in order to resolve a remaining degree of freedom (Andrews, 1986), a reference condition either for the source or site part needs to be set. A common such reference is to fix the site response of a single or the average of a set of rock sites to be equal to unity, independent of frequency. However, if not only the relative site terms (i.e., amplification relative to the given reference condition), but also the absolute source spectra derived in the inversion are of interest, extreme care must be taken that this reference condition is reasonably chosen, in order to avoid bias in the source spectral shape. Particularly in Canterbury this is a difficult issue since most rock stations exhibit their own site response (van Houtte et al., 2012). In order to choose an appropriate reference condition, we therefore took into consideration the geological setting of the sites and the shape of the H/V ratios (calculated directly from the amplitude spectra used in the inversions), as well as the results from a range of trial runs using various reference conditions. Since (a) the NZNSN stations MQZ and RPZ (Figure 1) are located on rock, (b) the H/V spectral ratios for these stations are reasonably flat over the entire frequency range of analysis and (c) trial runs

with these stations provided results with reasonable spectral shapes of the source and site terms in the inversion, we came to the conclusion that imposing the average of the site response at these two stations to be equal to one is the most appropriate choice for our purposes. It should be noted at this point that imposing a well-founded reference condition is of crucial importance, since the site response functions of all other sites as well as the source spectra resulting from the inversion will be relative to the imposed constraint. Therefore, if an inappropriate reference condition were to be chosen, all the source spectra would show a systematic bias due to site amplification peaks or troughs of the reference site(s) not taken into account in the reference condition. The influence of potential high-frequency diminution effects, which are commonly parameterized by an exponential term $\exp(-\pi\kappa f)$ (e.g., Anderson and Hough, 1984), will be discussed in the following section. Finally, uncertainty estimates on the various non-parametric components are derived by running a set of 100 bootstrap inversions (Oth et al., 2011).

Figure 4 shows two examples for the site response functions derived under this reference condition assumption as well as an example for the 1D attenuation models obtained. As one would expect, the deep soil site shows a lower fundamental frequency (~2 Hz) than the shallow soil site (~3-4 Hz) as well as high-frequency de-amplification. In terms of attenuation, at each analyzed frequency, the spectral data points corrected for their source and site contributions follow the 1D- attenuation curves very well, showing that these are well-constrained by the data. The site response functions and non-linear soil behavior issues, as well as the attenuation characteristics will be discussed in detail in a dedicated article, and in the following, we will concentrate on the source components.

4. SOURCE SPECTRA AND STRESS DROP CALCULATION

The isolated non-parametric $S_i(f, M_i)$ terms represent the earthquake acceleration source spectra at the reference distance R_0. These are not subject to any specific assumption about functional form in terms of either attenuation or source spectral shape, and can be interpreted in the framework of an appropriate earthquake source model. However, as mentioned previously, their spectral shape is dependent on the reliability of the constraint assumed for the site response of the reference station(s).

Figure 5 shows four examples of these source spectra (black lines, gray shaded area denotes standard deviation from bootstrap analysis). While for instance the source spectrum of the M_W 7.2 Darfield event is nearly entirely flat over the bandwidth of analysis, those of the smaller events (Figure 5c and d) show an increase at low frequencies approximately proportional to f^2 and a plateau at high frequencies, consistent with the ω^{-2} source model (Aki, 1967). Indeed, fitting the ω^{-2}-model (Brune, 1970; Brune, 1971) to the inverted source spectra using the following equation (Oth et al., 2010):

$$S(f) = (2\pi f)^2 \frac{R^{\theta\varphi} VF}{4\pi\rho v_S^3 R_0} M(f) \text{ , with } M(f) = \frac{M_0}{1 + (f/f_C)^2} \text{ ,} \tag{3}$$

we can see that the ω^{-2} source model provides an excellent fit to the source spectra (Figure 5, dashed black lines). In equation (3), $M(f)$ denotes the moment rate spectrum, $R^{\theta\varphi}$ represents the average radiation pattern of S-waves set to 0.55 (Boore and Boatwright, 1984), $R_0=5$ km is the reference distance, $V = 1/\sqrt{2}$ accounts for the separation of S-wave energy onto two horizontal components, $F = 2$ is the free surface factor and ρ and v_S are density and shear wave velocity estimates in the source region, for which we adopted standard upper crustal density of $\rho = 2.7$ g/cm^3 and $v_S = 3.3$ km/s (derived from the 3D

velocity model of Fry et al., 2013). With this fitting procedure (using non-linear least squares), we determine the seismic moment M_0 (respectively moment magnitude M_W, Hanks and Kanamori, 1979) and corner frequency f_C for each earthquake. One restriction in this procedure applies to the larger events of $M_{W,GeoNet} \geq 5.5$: for such events, f_C is likely to be smaller than the lowest frequency of our analysis bandwidth, and in this case, it is impossible to reliably determine M_0 and f_C simultaneously (Oth et al., 2010). For this reason, we constrained M_0 to the value given in the GeoNet database for those events, which is well constrained by regional moment tensor inversion. Because of the necessity of constraining the moments for the largest events, it is important to ensure that the M_W values derived from the spectral fits are consistent with the $M_{W,GeoNet}$ values, since otherwise the scaling trend discussed below might be biased due to inconsistencies between the magnitudes of large and small events (Oth, 2013, see also Figure 9).

A further noteworthy observation is that the source spectra do not show any significant decay at high frequencies. It is well known that the Fourier amplitude spectra of ground motion records usually show a decay at high frequencies that can be approximated with an exponential of the form $\exp(-\pi\kappa f)$. This κ term is often associated with near-surface attenuation at the observation sites (Anderson and Hough, 1984; Boore, 2003) and therefore often considered a site effect, even though some path and source contributions to this high-frequency diminution effect are also under debate (e.g., Hanks, 1982; Papageorgiou and Aki, 1983). Oth et al. (2011) showed that a site-related κ effect at the reference site, if not taken into account when imposing the reference constraint, can be systematically moved into the source spectra and may need to be taken into account during their interpretation.

Path-related high-frequency diminution effects, in contrast, will flow into the general attenuation effects that lead to the non-parametric attenuation curves $A(f, R_{ij})$.

Since indeed the reference condition in our inversion does not include such a κ decay, one might expect that the high-frequency diminution effect related to the reference site(s) is moved into the source spectral estimates, as was previously observed in Japan (Oth et al., 2011). This effect, if present, needs to be corrected in the framework of a source spectral interpretation within the ω^{-2} model. In order to quantify how strongly this issue might affect our source spectral estimates at high frequencies, we systematically calculate κ for our source spectra by fitting the following relation to the high-frequency part:

$$\log_{10} S_i(f > f_E) = S_{0,i} - \log_{10} e \cdot \pi \kappa_i f , \tag{4}$$

with f_E being the lower frequency bound considered (Anderson and Hough, 1984). In view of the magnitude range of the events considered in this study, we set $f_E = 10$ Hz in order to be well beyond the corner frequency range of the events (Parolai and Bindi, 2004), but strictly speaking, f_E would have to be appropriately chosen for each individual spectrum.

The distribution of source κ values is shown in Figure 6. The obtained values are very small, with an average of 0.006 sec, and roughly normally distributed. These values are in contrast to the rock site value of 0.03 sec found in the source spectra obtained by Oth et al. (2011) in Japan and thus mean that the reference site condition of unity imposed on the average of the sites MQZ and RPZ does not introduce a significant high-frequency diminution effect in the source spectra. Instead this implies that this effect, if present, must have been completely taken up in the attenuation operator $A(f, R_{ij})$. In Figure 5, the white circles at high frequencies represent the high-frequency source spectra (for frequencies

12

higher than 10 Hz) following the automatic κ-correction, showing that the effect is overall negligible in the case of the Canterbury dataset.

Stress drop estimates $\Delta\sigma$ are computed based on the determined M_0 and f_C values following Hanks and Thatcher (1972):

$$\Delta\sigma = 8.5\, M_0 \left(\frac{f_C}{v_S}\right)^3 . \qquad (5)$$

These stress drop values relate to the model introduced by Brune (1970, 1971), and it should be noted here that using a different model, such as the well-known Madariaga (1976) one, will result in different stress drop values (higher by a factor of 5.5 in the case of the Madariaga model). Therefore, before comparing stress drop estimates from different studies, consistency in terms of underlying model assumptions should imperatively be verified. Also note that the link between stress drop and the so-called apparent stress, which is commonly determined through integration of the earthquake source spectrum and is directly related to an estimate of the radiated energy of the earthquake, is given via the assumed source model. For source spectra that are well characterized by the ω^{-2}-model, proportionality between these two quantities is expected (see for instance Singh and Ordaz 1994). However, this is not necessarily always the case, and the terms *apparent stress* and *stress drop* are not simply interchangeable.

In order to provide an uncertainty estimate of seismic moment M_0, corner frequency f_C and stress drop $\Delta\sigma$, we follow the approach of Viegas et al. (2010). This involves determining the bounds of the range of values for M_0 and f_C where the variance of the best fit between the observed and theoretical source spectrum increases by 5%.

One final concern that might be raised lies in the fact that the attenuation model considered in this work is only 1D. If strong 2D/3D attenuation heterogeneities were present in the vicinity of the source zones, they could in principle be mapped into the source spectra and lead to biased stress drop estimates, such that any lateral stress drop variations would rather represent lateral attenuation variations. While such a trade-off between source spectral level and attenuation characteristics can never be fully excluded, we can test whether or not the data points from events with different stress drop ranges show any systematic differences relative to the 1D attenuation model derived from the entirety of the dataset. At a given frequency, source spectral level is not distant-dependent whereas attenuation definitely is, and therefore, differing trends in the distance-dependence of data points from earthquakes with very low or very high stress drops might be expected if such a trade-off was to bias the source spectra. Figure 7 shows that source- and site-corrected data points from events with different stress drop levels follow the attenuation model overall equally well, both at low and high frequency. It is only at the largest distances that data points from the lowest and highest stress drop events (lowest and highest 5% of stress drop distribution) show some slight deviation. However, these data points are only very few and are thus statistically not relevant. Therefore, this test does not provide any indication that 2D/3D attenuation effects not taken into account would significantly bias the stress drops determined in this work.

5. RESULTS AND DISCUSSION

Stress drop is the source parameter governing high-frequency energy radiation during earthquakes and, as such, is a key parameter for ground motion prediction and seismic hazard assessment. In this context, its variability in particular is of great importance (Cotton

et al., 2013). Studies involving large datasets on global scales or covering large regions usually come to the conclusion that stress drop varies over at least three orders of magnitude, if not more (e.g., Shearer et al., 2006; Allmann and Shearer, 2007; Oth et al., 2010).

Figures 5c and d provide an excellent illustration of the effect of varying stress drop of two earthquakes with nearly the same seismic moment. While the low-frequency asymptote is nearly the same for these two events, showing that they have approximately identical seismic moments, their corner frequencies and high-frequency plateau levels vary considerably. The event in Figure 5d has almost one order of magnitude higher stress release (~9.5 MPa) than the one in Figure 5c (~1.5 MPa) and is hence significantly more energetic.

Stress drops of the Canterbury earthquakes vary between about 1 to 20 MPa (Figure 8), thus covering a little more than one order of magnitude variability. This is considerably less than the above-mentioned overall scatter of at least three orders of magnitude observed on large-scale datasets. This observation of lower stress release variability in individual earthquake sequences has also been made in Japan (Oth, 2013) and provides indications that on local (regional) scales, stress release variability is only of about one order of magnitude. However, significant variations in the average stress drop level between different areas exist. In Canterbury, the median of the stress drop distribution is about 5 MPa (Figure 8b), which is high compared to other regions where stress drops of crustal earthquakes have been derived using the methodology applied in this study. For crustal earthquakes in Japan for instance, a median stress drop of only ~1 MPa was obtained (Oth et al., 2010), whereas for the L'Aquila sequence in Italy, the average stress drop ranged around 3 MPa (Ameri et al., 2011, all calculated using the same source model). The high

stress drops of Canterbury earthquakes obtained here are in good agreement with previous findings of high apparent stress or implied stress drop (Fry and Gerstenberger, 2011; Holden, 2011) and most likely reflect the fact that these earthquakes take place in an immature intra-plate setting, with little seismic activity prior to this sequence. As noted by Fry and Gerstenberger (2011), the Canterbury events are most likely taking place on strong faults characterized by high friction. In contrast, Japan is overall characterized by much higher seismicity rates and therefore also by more mature crustal features. However, in contrast to the apparent stress results of Fry and Gerstenberger (2011) that are based on teleseismically estimated radiated energy calculations, we obtain larger stress drop for the M_W 6.2 Christchurch event than for the M_W 7.2 Darfield one. A potential explanation for this fact could lie in the focal mechanism correction applied in the methodology of Choy and Boatwright (1995) for calculating radiated energy. As noted by Di Giacomo et al. (2010), teleseismic energy magnitude estimates of strike-slip earthquakes including this correction are systematically higher by about 0.2-0.3 magnitude units than those without, and this is only the case for strike-slip events. Notwithstanding this issue, this study clearly corroborates that stress drops in Canterbury are indeed higher than in other, higher-strain-rate, regions.

As mentioned earlier, stress drop scaling with earthquake size is a key aspect in seismic hazard assessment. In particular, if earthquakes scale self-similarly with seismic moment, stress drop is constant and $M_0 \propto f_C^{-3}$ (Aki, 1967). Indeed, datasets involving large earthquake populations usually do not find a significant deviation from this scaling rule (e.g., Shearer et al., 2006; Allmann and Shearer, 2007; Oth et al., 2010). However, the findings of some studies on individual earthquake sequences indicate that significant breaks in self-similarity may occur (e.g., Mayeda and Malagnini, 2010), even though contradictory

results have been obtained for the same earthquake sequences (Baltay et al., 2010). Kanamori and Rivera (2004) proposed to quantify deviations from the self-similarity principle through the so-called ε parameter, such that $M_0 \propto f_C^{-(3+\varepsilon)}$. With this parameterization, $\varepsilon=0$ in the case of self-similar scaling, while $\varepsilon>0$ indicates increasing stress drop with earthquake size and $\varepsilon<0$ results in the opposite trend.

The scaling characteristics of the Canterbury earthquake sequence are shown in Figure 9a in the form of an $M_0 - f_C$ plot. In the framework of the uncertainty estimates calculated following the approach of Viegas et al. (2010), the corner frequencies and seismic moments are robustly constrained for almost all events. The determination of ε results in the value $\varepsilon = 0.16\pm0.17$, where the uncertainty range given is the standard deviation resulting from a bootstrap analysis of 100 resampled datasets. This result indicates that, if any, there is only a very weak increase of stress drop with seismic moment, and self-similarity is certainly an option within the uncertainty bounds. As indicated in the previous section, it is important that the moment magnitudes of the small/moderate events derived from the spectral fitting procedure are consistent with the ones fixed for the larger shocks. Figure 9b shows the comparison of $M_{W,GeoNet}$ and $M_{W,spectral\ fit}$. In the M_W range 4-5, the $M_{W,GeoNet}$ values tend to be slightly larger than the values derived from the spectral fit, while for the smallest events, this trend reverses. However, the differences are well within 0.1 magnitude units in most cases, and thus we conclude that overall, the seismic moments determined for the small/moderate events are compatible with the values set for the large ones. Therefore, we do not expect any significant bias of the scaling results in that respect.

Finally, an important aspect of stress drop variability lies in the question of whether there are systematic lateral variations. Figure 10 shows the stress drop measurements as

given in Figure 8a in map view. There are several noteworthy clusters appearing in the evolution of the Canterbury sequence (Bannister and Gledhill, 2012). The M_W 7.2 complex Darfield mainshock rupture began on a subsidiary thrust fault, with a hypocenter about 4 km north of the near-vertical strike-slip Greendale Fault that represents the main part of the rupture (Gledhill et al., 2011). Aftershock activity decayed relatively rapidly in the zone extending to the west and north of the Greendale fault, whereas aftershocks clustered persistently at the eastern edge of the Greendale fault, including a significant number of moderate events immediately following the Darfield rupture (Bannister and Gledhill, 2012). On 22 February 2011, the M_W 6.2 oblique-reverse Christchurch event occurred. Aftershock activity was triggered throughout the entire Canterbury region, but particularly pronounced in the vicinity of the M_W 6.2 epicenter. The M_W 6.0 June 2011 event, involving right-lateral strike-slip motion, occurred on a fault plane thought to intersect the eastern edge of the fault plane associated with the February event, and was in turn followed by the reverse faulting M_W 5.9 December 2011 event offshore. Overall, strike-slip faulting dominated along the trace of the Greendale Fault and its eastern edge, while some reverse faulting mechanisms are apparent to the west and north of the aftershock zone, as well as offshore following the M_W 5.9 December earthquake (Ristau et al., 2013). Oblique mechanisms are dominant throughout much of the vicinity of Christchurch city (Gledhill et al., 2011).

In terms of stress drop variations, these clusters show interesting features (Figure 10). The M_W 7.2 Darfield mainshock shows a slightly elevated stress drop compared to the average, which, in view of the significant uncertainties that are generally associated with stress drop estimates, should however not be over-interpreted. We also note at this point that the stress drop estimate for the Darfield event showed a non-negligible dependence on the maximum window length allowed in the calculation of the spectra (increasing with

18

increasing window length up to about 20 sec). We therefore allowed for a maximum of 20-second window length, since allowing windows longer than this did not significantly increase the stress drop further. However, a non-negligible portion of surface wave energy in addition to S-wave energy may therefore be included in the spectra, and therefore the stress drop estimate for the Darfield event should most probably be considered as an upper bound estimate. As a general rule, stress drop estimates determined from the spectra of such large events as the Darfield one, involving complex ruptures, are to be interpreted with caution. For aftershocks of the Darfield event, stress drops were particularly high in the cluster at the eastern edge of the Greendale Fault.

Before moving on to the M_W 6.2 Christchurch event and its aftershocks, we also remind the reader once more of the uncertainties that stress drop calculations always involve. Indeed, besides the error estimates derived from the regression analysis of the inverted source spectra (which indicate that the source spectra can robustly be modeled as ω^{-2} sources, see Figure 8a), other effects that are more difficult to quantify should not be forgotten, such as potential trade-offs between source terms and near-source attenuation, or between source and site terms. As discussed in the previous section, near-source attenuation variations could in principle bias the observed stress drop variations. We investigated this possibility (Figure 7) and could not find any significant hints for such a bias. Due to the fact that each station recorded multiple events and each event was recorded at multiple stations, the most significant danger for a trade-off between source and site terms comes from the choice of an inappropriate reference condition, and as discussed in section 3, we are confident for several reasons that our choice is reasonable. The source spectra also do not show any significant peaks or troughs that would hint towards a contamination with a residual site response effect. Nevertheless, spectrally determined stress drop estimates

inherently involve many factors of uncertainty, and these should be kept in mind during the discussion.

While the M_W 6.2 Christchurch event shows very high stress release, a notable feature is the comparatively low stress drops of aftershocks in two clusters in its vicinity (marked by white ellipses (black ellipses in the inset) in Figure 10). The cluster to the north (less than 2 km away from the Christchurch city center) actually occurred well before the M_W 6.2 event in February 2011, starting with a M_W 4.7 event on 26 December 2010 that caused significant damage. This earthquake was followed by a sequence including two more events of magnitude larger than 4 within a couple of hours (this sequence was termed the *Boxing day earthquakes*) and a series of events in the vicinity within the following 3-4 weeks. Similarly, the aftershocks of the M_W 6.2 February 2011 Christchurch event southwest of its epicenter (partially within the southwestern part of the estimated fault plane projection for the M_W 6.2 event, see inset of Figure 10) are also consistently lower stress drop, and are clearly distinguished from the higher stress drops to the east as well as at the eastern edge of the Greendale Fault.

A cluster of high stress drop events also followed the 2011 February M_W 6.2 event and is located between the estimated source areas of the 2011 February and the 2011 June (M_W 6.0) events (inset of Figure 10). This cluster stands in contrast to the lower stress drop aftershocks of the 2011 February event to the southwest of the rupture plane mentioned previously. This apparent clustering of high stress drop aftershocks both east of the Greendale Fault and east of the M_W 6.2 Christchurch event may point to stress concentration effects at the rupture edges of these events as a result of loading due to their rupture processes. Such effects are not easily discernible for the 2011 June event, where some high stress drop aftershocks occur well within the assumed rupture plane projection

20

(Figure 10, inset). However, it should also be noted that the extent of the 2011 June event fault plane is not well constrained (Beavan et al., 2012). In order to shed light on the lateral stress drop pattern of the 2011 June event's aftershocks and to better constrain the evolution of the stress drop offshore following the M_W 5.9 December 2011 event, the inclusion of more events in this area is necessary in the future. Apart from these apparent clusters of high and low stress drop mentioned above, we could not find an evident temporal change of average stress drop level among earthquakes occurring before and after the M_W 6.2 Christchurch and the 2011 M_W 6.0 June event in their respective surroundings, in agreement with the findings of Shearer et al. (2006) in southern California.

6. CONCLUSIONS

In this study, we investigated the stress release of the Canterbury earthquake sequence within the magnitude range M_W 3 – 7.2, taking advantage of the availability of a very dense set of recordings from the GeoNet strong motion database. This earthquake sequence provides a unique opportunity to improve our understanding of the stress release mechanisms of earthquakes in low-seismicity regions.

We showed that the source spectra of the Canterbury sequence are very well characterized by the ω^{-2} model, with on average close to self-similar scaling of stress drop with earthquake size. Furthermore, the Canterbury earthquakes are characterized by high stress drops, in the range 1 – 20 MPa, with a median of ~5 MPa. These values are high compared to more seismically active regions such as Japan, as a result of the Canterbury events taking place on more immature crustal features (a similar analysis to the one presented in this article using the same methods determined a median stress drop for crustal earthquakes in Japan of the order of 1 MPa, Oth et al., 2010; Oth, 2013). Of the larger

earthquakes in the sequence, the M_W 6.2 Christchurch event that occurred in February 2011 was particularly energetic, which in addition to other factors such as directivity and site effects, certainly played a key role in its destructiveness. Lateral variations in stress drops during the aftershock sequence indicate that higher stress events seem to occur at the edges of major fault planes.

In contrast to large-scale earthquake populations (global or covering large regions) that show stress drop variations over three orders of magnitude, the Canterbury sequence stress drops show variation over little more than one order of magnitude. This variability range is in good agreement with the results derived for individual earthquake sequences in Japan (Oth, 2013) and implies that the stress release variability on local/regional scales (such as in Canterbury) is much smaller than the three orders of magnitude obtained from global/large area datasets. This means that narrower variability ranges, centered on appropriate regional average stress drop values, can be used for ground motion prediction and hazard assessment.

Acknowledgments

REFERENCES

Aki, K. (1967). Scaling law of seismic spectrum. J. Geophys. Res. *72*, 1217-1231, doi: 10.1029/JZ072i004p01217.

Allmann, B.P., and Shearer, P.M. (2007). Spatial and temporal stress drop variations in small earthquakes near Parkfield, California. J. Geophys. Res. *112*, B04305, doi: 10.1029/2006JB004395.

Ameri, G., Oth, A., Pilz, M., Bindi, D., Parolai, S., Luzi, L., Mucciarelli, M., and Cultrera, G. (2011). Separation of source and site effects by generalized inversion technique using the aftershock recordings of the 2009 L'Aquila earthquake. Bull. Earthq. Eng. *9*, 717-739, doi: 10.1007/s10518-011-9248-4.

Anderson, J.G., and Hough, S.E. (1984). A model for the shape of the Fourier amplitude spectrum of acceleration at high frequencies. Bull. Seismol. Soc. Am. *74*, 1969-1993.

Andrews, D.J. (1986). Objective determination of source parameters and similarity of earthquakes of different size. In Earthquake Source Mechanics, S. Das, J. Boatwright, and C.H. Scholz, eds. (Washington DC: American Geophysical Union).

Baltay, A., Prieto, G., and Beroza, G.C. (2010). Radiated seismic energy from coda measurements and no scaling in apparent stress with seismic moment. J. Geophys. Res. *115*, B08314, doi: 10.1029/2009JB006736.

Bannister, S., and Gledhill, K. (2012). Evolution of the 2010-2012 Canterbury earthquake sequence. New Zealand J. Geol. Geophys. *55*, 295-304, doi: 10.1080/00288306.2012.680475.

Beavan, J., Motagh, M., Fielding, E.J., Donnelly, N., and Collett, D. (2012). Fault slip models of the 2010–2011 Canterbury, New Zealand, earthquakes from geodetic data and observations of postseismic ground deformation. New Zealand J. Geol. and Geophys., *55*, 207-221.

Boore, D.M. (2003). Simulation of ground motion using the stochastic method. Pure Appl. Geophys. *160*, 635-676.

Boore, D.M., and Boatwright, J. (1984). Average body-wave radiation coefficients. Bull. Seismol. Soc. Am. *74*, 1615-1621.

Bradley, B.A. (2012). Strong ground motion characteristics observed in the 4 September 2010 Darfield, New Zealand earthquake. Soil Dyn. Earthq. Eng. *42*, 32-46, doi: 10.1016/j.soildyn.2012.06.004.

Brune, J.N. (1970). Tectonic stress and the spectra of seismic shear waves from earthquakes. J. Geophys. Res. *75*, 4997-5009.

Brune, J.N. (1971). Correction. J. Geophys. Res. *76*, 5002.

Castro, R.R., Anderson, J.G., and Singh, S.K. (1990). Site response, attenuation and source spectra of S waves along the Guerrero, Mexico, subduction zone. Bull. Seismol. Soc. Am. *80*, 1481-1503.

Choy, G.L., and Boatwright, J.L. (1995). Global patterns of radiated seismic energy and apparent stress. J. Geophys. Res. *100*, 18205-18228.

Cotton, F., Archuleta, R., and Causse, M. (2013). What is Sigma of the Stress Drop? Seismol. Res. Lett. *84*, 42-48, doi: 10.1785/0220120087.

Di Giacomo, D., Parolai, S., Bormann, P., Grosser, H., Saul, J., Wang, R., and Zschau, J. (2010). Suitability of rapid energy magnitude determinations for emergency response purposes. Geophys. J. Int. *180*, 361-374, doi: 10.1111/j.1365-246X.2009.04416.x.

Fry, B., and Gerstenberger, M.C. (2011). Large Apparent Stresses from the Canterbury Earthquakes of 2010 and 2011. Seismol. Res. Lett. *82*, 833-838, doi: 10.1785/gssrl.82.6.833.

Fry, B., Benites, R., and Kaiser, A. (2011). The Character of Accelerations in the Mw 6.2 Christchurch Earthquake. Seismol. Res. Lett. *82*, 846-852, doi: 10.1785/gssrl.82.6.846.

Fry, B., Eberhart-Phillips, D., and Davey, F. (2013). Mantle accommodation of lithospheric shortening as seen by combined interferometry and body-wave imaging in the South Island, New Zealand, submitted to Geophys. J. Int.

Gledhill, K., Ristau, J., Reyners, M., Fry, B., and Holden, C. (2011). The Darfield (Canterbury, New Zealand) Mw 7.1 Earthquake of September 2010: A Preliminary Seismological Report. Seismol. Res. Lett. *82*, 378-386, doi: 10.1785/gssrl.82.3.378.

Haines, A.J. (1981). A local magnitude scale for New Zealand earthquakes. Bull. Seismol. Soc. Am. *71*, 275-294.

Hanks, T.C. (1982). fmax. Bull. Seismol. Soc. Am. *72*, 1867-1879.

Hanks, T.C., and Kanamori, H. (1979). A moment magnitude scale. J. Geophys. Res. *84*, 2348-2350.

Hanks, T.C., and Thatcher, W. (1972). A graphical representation of seismic source parameters. J. Geophys. Res. *77*, 4393-4405.

Holden, C. (2011). Kinematic Source Model of the 22 February 2011 Mw 6.2 Christchurch Earthquake Using Strong Motion Data. Seismol. Res. Lett. *82*, 783-788, doi: 10.1785/gssrl.82.6.783.

Irikura, K. (1986). Prediction of strong acceleration motion using empirical Green's function. Proceedings of 7th Japan Earthquake Engineering Symposium , 151-156.

Kaiser, A., Holden, C., Beavan, J., Beetham, D., Benites, R., Celentano, A., Collett, D., Cousins, J., Cubrinovski, M., Dellow, G., Denys, P., Ficlding, E., Fry, B., Gerstenberger, M., Langridge, R., Massey, C., Motagh, M., Pondard, N., McVerry, G., Ristau, J., Stirling, M., Thomas, J., Uma, S.R., and Zhao, J. (2012). The Mw 6.2 Christchurch earthquake of February 2011: Preliminary report. New Zealand J. Geol. Geophys. *55*, 67-90, doi: 10.1080/00288306.2011.641182.

Kanamori, H., and Rivera, L. (2004). Static and dynamic scaling relations for earthquakes and their implications for rupture speed and stress drop. Bull. Seismol. Soc. Am. *94*, 314-319.

Konno, K., and Ohmachi, T. (1998). Ground-motion characteristics estimated from spectral ratio between horizontal and vertical components of microtremor. Bull. Seismol. Soc. Am. *88*, 228-241.

Madariaga, R. (1976). Dynamics of an expanding circular fault. Bull. Seismol. Soc. Am. *66*, 639-666.

Mayeda, K., and Malagnini, L. (2010). Source radiation invariant property of local and near-regional shear-wave coda: Application to source scaling for the Mw 5.9 Wells, Nevada sequence. Geophys. Res. Lett. *37*, L07306, doi: 10.1029/2009GL042148.

Menke, W. (1989). Geophysical Data Analysis: Discrete Inverse Theory (New York: Academic Press).

Orense, R.P., Kiyota, T., Yamada, S., Cubrinovski, M., Hosono, Y., Okamura, M., and Yasuda, S. (2011). Comparison of liquefaction features observed during the 2010 and 2011 Canterbury earthquakes. Seismol. Res. Lett. *82*, 905-918, doi: 10.1785/gssrl.82.6.905.

Oth, A., Bindi, D., Parolai, S., and Di Giacomo, D. (2010). Earthquake scaling characteristics and the scale-(in)dependence of seismic energy-to-moment ratio: Insights from KiK-net data in Japan. Geophys. Res. Lett. *37*, L19304, doi: 10.1029/2010GL044572.

Oth, A., Bindi, D., Parolai, S., and Di Giacomo, D. (2011). Spectral Analysis of K-NET and KiK-net Data in Japan, Part II: On Attenuation Characteristics, Source Spectra, and Site Response of Borehole and Surface Stations. Bull. Seismol. Soc. Am. *101*, 667-687, doi: 10.1785/0120100135.

Oth, A., Parolai, S., and Bindi, D. (2011). Spectral Analysis of K-NET and KiK-net Data in Japan, Part I: Database Compilation and Peculiarities. Bull. Seismol. Soc. Am. *101*, 652-666, doi: 10.1785/0120100134.

Oth, A. (2013). On the characteristics of earthquake stress release variations in Japan. Earth Planet. Sci. Lett., 377-378, 132-141, doi: 10.1016/j.epsl.2013.06.037.

Papageorgiou, A.S., and Aki, K. (1983). A specific barrier model for the quantitative description of inhomogeneous faulting and the prediction of strong ground motion. Part I. Description of the model. Bull. Seismol. Soc. Am. *73*, 693-722.

Parolai, S., and Bindi, D. (2004). Influence of soil-layer properties on k evaluation. Bull. Seismol. Soc. Am. *94*, 349-356.

Petersen, T., Gledhill, K., Chadwick, M., Gale, N.H., and Ristau, J. (2011). The New Zealand National Seismograph Network. Seismol. Res. Lett. *82*, 9-20, doi: 10.1785/gssrl.82.1.9.

Quigley, M., Villamor, P., Furlong, K., Beavan, J., Van Dissen, R., Litchfield, N., Stahl, T., Duffy, B., Bilderback, E., Noble, D., Barrell, D., Jongens, R., and Cox, S. (2010). Previously Unknown Fault Shakes New Zealand's South Island. Eos Trans. AGU *91*, 49.

Ristau, J. (2008). Implementation of Routine Regional Moment Tensor Analysis in New Zealand. Seismol. Res. Lett. *79*, 400-415, doi: 10.1785/gssrl.79.3.400.

Ristau, J. (2013). Update of Regional Moment Tensor Analysis for Earthquakes in New Zealand and Adjacent Offshore Regions, *Bull. Seismol. Soc. Am.,* **103,** in press.

Ristau, J., Holden, C., Kaiser, A., Williams, C., Bannister, S., and Fry, B. (2013). The Pegasus Bay aftershock sequence of the Mw 7.1 Darfield (Canterbury), New Zealand earthquake. Submitted to Geophys. J. Int.

Shearer, P.M., Prieto, G.A., and Hauksson, E. (2006). Comprehensive analysis of earthquake source spectra in southern California. J. Geophys. Res. *111*, B06303, doi: 10.1029/2005JB003979.

Singh, S.K., and Ordaz, M. (1994). Seismic energy release in Mexican subduction zone earthquakes. Bull. Seismol. Soc. Am. *84*, 1533-1550.

van Houtte, C., Ktenidou, O.-J., Larkin, T., and Kaiser, A. (2012). Reference stations for Christchurch. Bull. New Zealand Soc. Earthq. Eng. *45*, 184-195.

Viegas, G., Abercrombie, R.E., and Kim, W.-Y. (2010). The 2002 M5 Au Sable Forks, NY, earthquake sequence: Source scaling relationships and energy budget. J. Geophys. Res. *115*, B07310, doi: 10.1029/2009JB006799.

Wallace, L.M., Beavan, J., McCaffrey, R., Berryman, K., Denys, P. (2007). Balancing the plate motion budget in the South Island, New Zealand using GPS, geological and seismological data. Geophys. J. Int. *168:* 332-352, doi: 10.1111/j.1365-246X.2006.03183.x
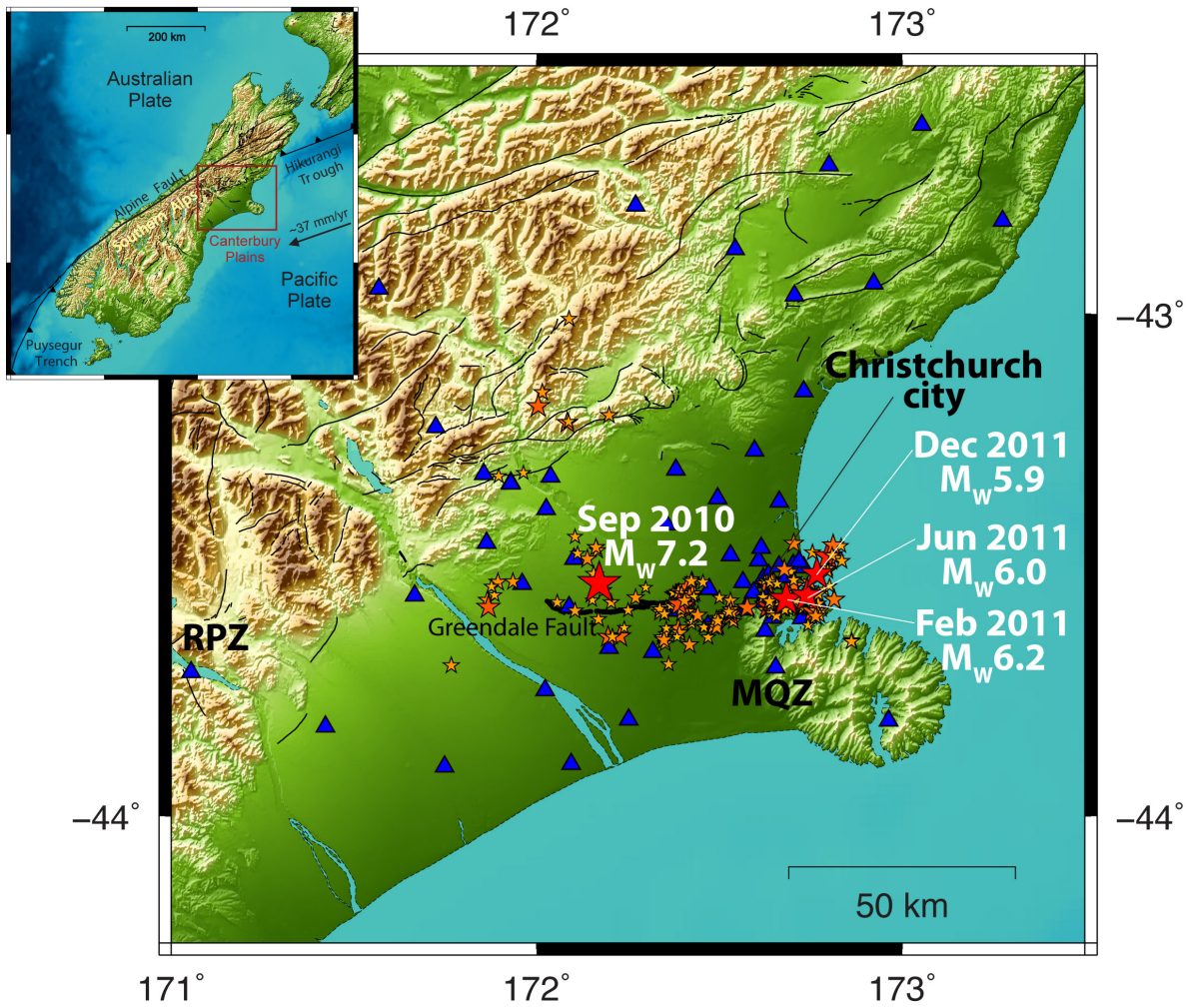
Figure 1: Epicenters of earthquakes (stars) and stations (blue triangles) used in this study.
Red stars indicate the September 2010 (M_W 7.2, Darfield earthquake), February 2011 (M_W
6.2, Christchurch earthquake), June 2011 (M_W 6.0) and December 2011 (M_W 5.9) shocks.
The Greendale fault (main fault involved in the 2010 Darfield event) is indicated as a black
line. Locations for the most significant events are derived from additional double difference
relocation analysis (e.g., Bannister and Gledhill, 2012).
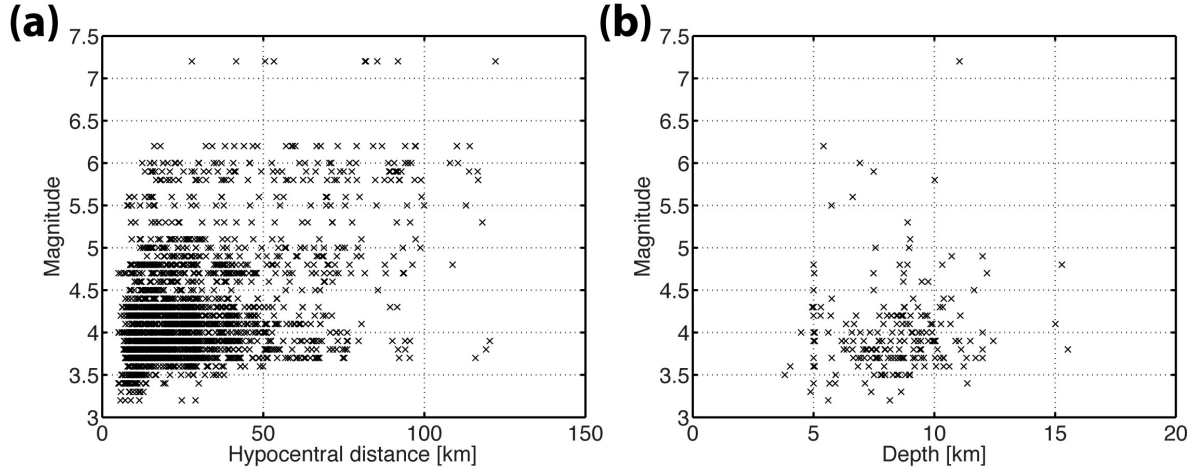
Figure 2: Dataset characteristics. (a) GeoNet moment magnitude ($M_{W,GeoNet}$) versus hypocentral distance. (b) Magnitude versus event depth.
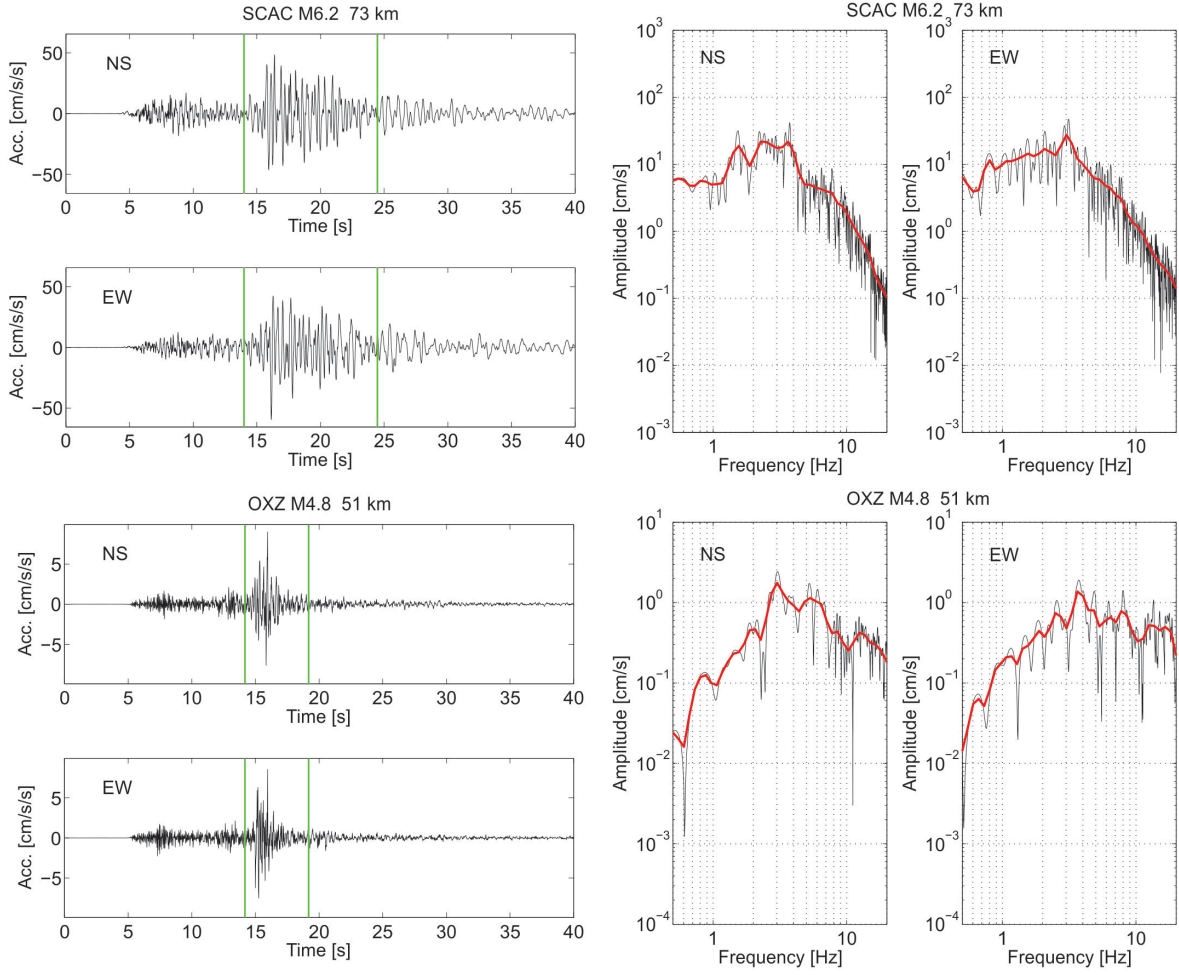
Figure 3: Examples of the event recordings. Top left: recording of the February 2011 Christchurch event (M_W=6.2) at station SCAC (NS and EW components, hypocentral distance 73 km). The green lines indicate the selected time window. Top right: corresponding Fourier amplitude spectra, red lines indicate the smoothed spectra using the Konno and Ohmachi (1998) filter with *b*=30. Bottom: same as top row for a moderate (M_W=4.8) earthquake located at a distance of 51 km from station OXZ.
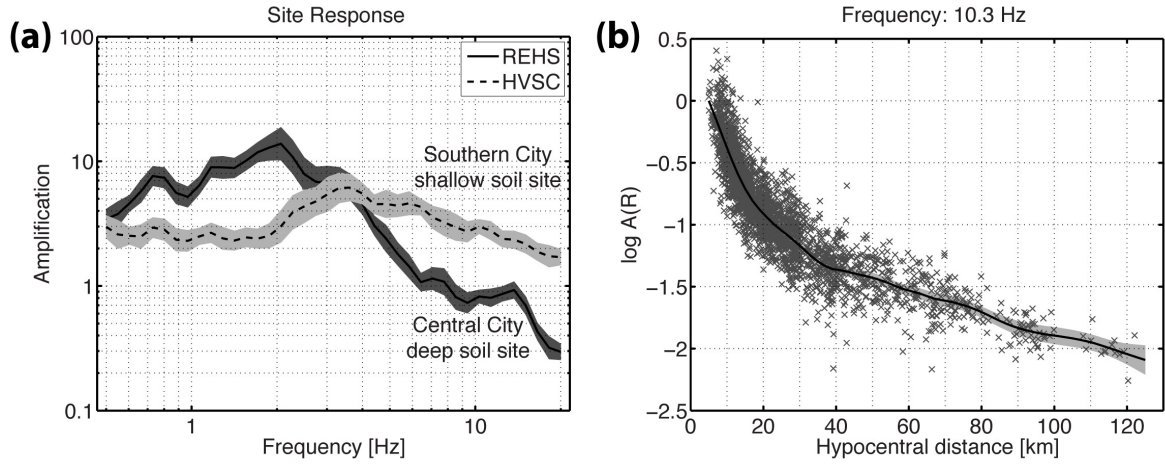
Figure 4: (a) Two examples of site response functions resulting from the spectral inversion. REHS is a deep soil site in the Christchurch central city, while HVSC is a shallow soil site in southern Christchurch. Note the lower predominant frequency for REHS as compared with the response at HVSC. (b) Example for the non-parametric attenuation curves at frequency 10.3 Hz (black line, gray shaded area denotes one standard deviation of the bootstrap analysis) and individual data points (corrected for source and site terms).
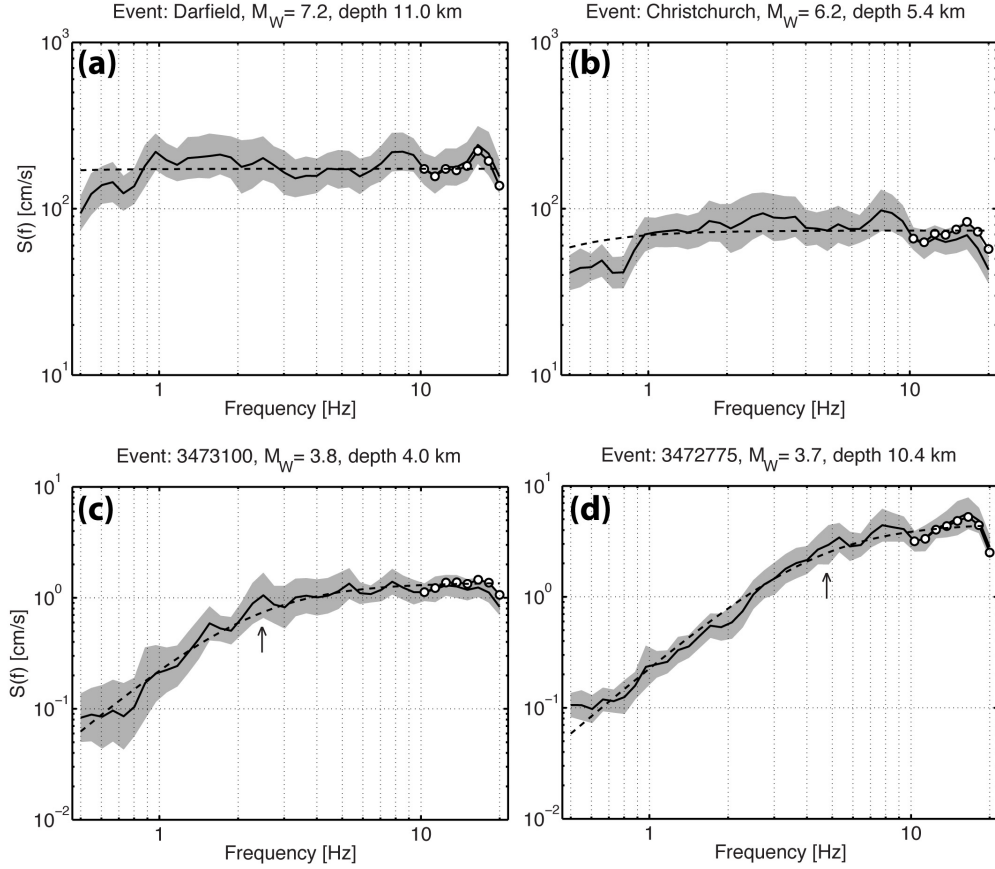
Figure 5: Four examples of acceleration source spectra derived from GIT inversion (black line: average; gray shaded area: standard deviation from bootstrap analysis) for four events. Dashed lines denote the best ω^{-2} source spectral fit. White dots at frequencies larger than 10 Hz show the high-frequency κ correction (Oth et al., 2011) (see also text and Figure 6), which only has a negligibly small effect in this dataset. (a) Source spectrum of the September 2010 Darfield earthquake, M_W 7.2. Note that the source spectrum is practically flat over the entire bandwidth of analysis, characteristic of an ω^{-2} source spectrum of a large earthquake with corner frequency lower than the lower bandwidth limit. (b) February 2011 Christchurch event, M_W 6.2. (c) and (d): Two examples for lower magnitude events. The events show an excellent fit with the ω^2-model and have nearly the same M_W, but very different corner frequencies (indicated by the arrows) and, consequently, stress drops.
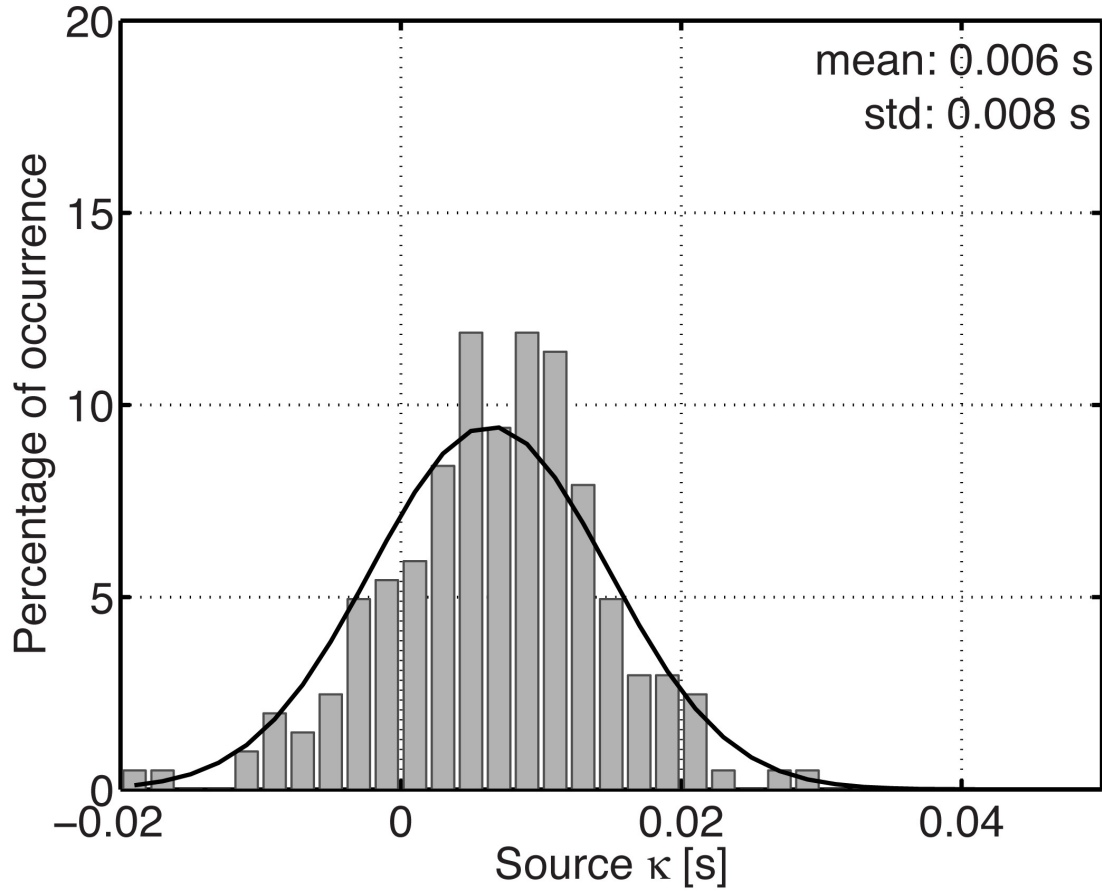
Figure 6: Distribution of residual high-frequency decay parameter κ in the source spectra, estimated from the high-frequency decay for f > 10 Hz. Most values are well below 0.02 s, indicating that also at highest frequencies the source spectra are approximately flat, as expected for ω^{-2} acceleration source spectra. The black line indicates the fit of a normal distribution function to the data.

(a) Frequency f=1 Hz

(b) Frequency f=10 Hz
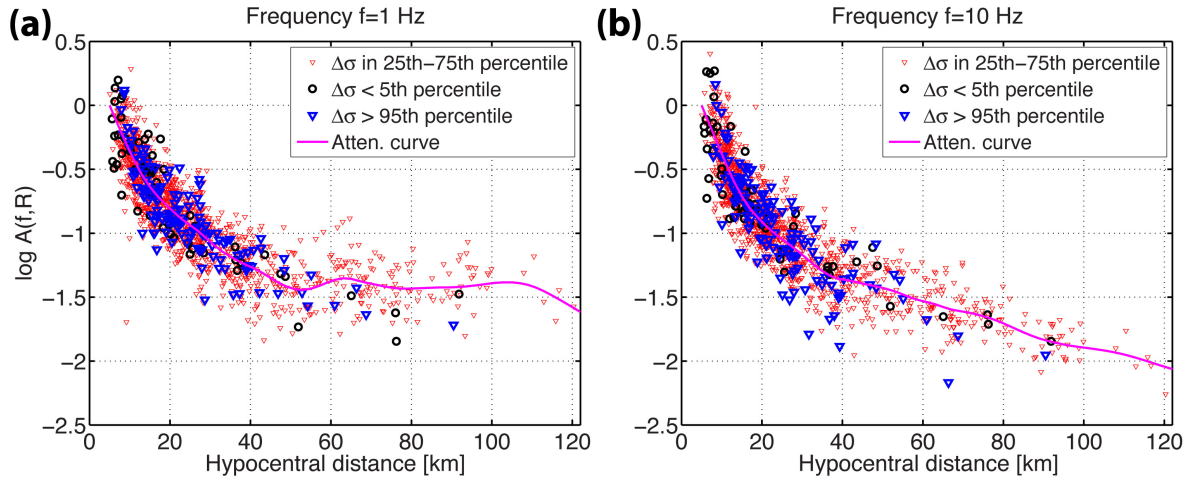
Figure 7: Comparison of source and site-corrected spectral amplitude decay with distance from earthquakes with different stress drop ranges and the inverted attenuation model at frequencies (a) 1 and (b) 10 Hz. Red triangles: data from moderate stress drop events within the interquartile range. Black circles: data from 5% lowest stress drop events. Blue triangles: data from 5% highest stress drop events. Magenta line: 1D attenuation model. Spectral amplitudes from events with different stress drop ranges follow the 1D attenuation model equally well. It is only at the largest distances that data points from the highest stress drop events could be slightly biased relative to the attenuation curve, but these data points are very few and thus have only very limited influence on the estimated stress drops.
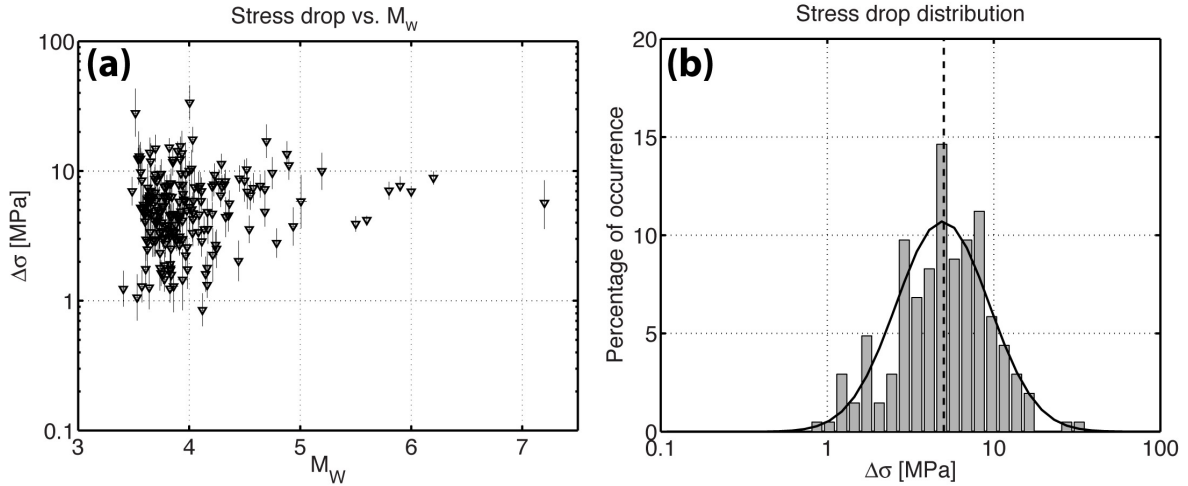
Figure 8: Stress drops of the 2010-2011 Canterbury sequence. (a) Stress drop versus magnitude. Uncertainty ranges are determined following the approach of Viegas et al. (2010). Values range from 1 to 20 MPa, with two outliers between 30 and 40 MPa at low magnitude. Note that the 2010 Darfield earthquake (largest event) shows a comparatively low stress drop relative to the 2011 February, June and December events (magnitude range 5.9 – 6.2). (b) Stress drop distribution as a histogram plot. Tentative log-normal fit to the distribution is overlain as black line. The median of the distribution (indicated by the dashed line) is ~5 MPa.
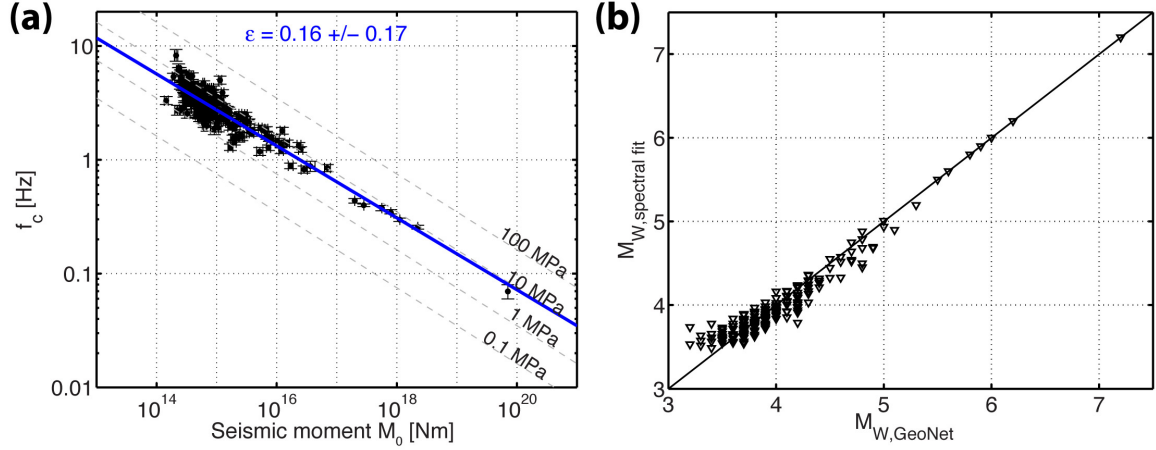
Figure 9: Scaling characteristics of the 2010-2011 Canterbury earthquake sequence. (a) f_C − M_0 plot, with constant stress drop values indicated by dashed lines. E is determined from the slope of the linear fit in log f_C − log M_0 (blue line), and the standard deviation is obtained from bootstrap resampling. (b) Comparison of M_W values derived from the spectral fitting procedure with the estimated GeoNet moment magnitudes, $M_{W,GeoNet}$ (see text for explanations). Note that for events with $M_{W,GeoNet} \geq 5.5$, the moment for the spectral fits is set according to this value (see text).
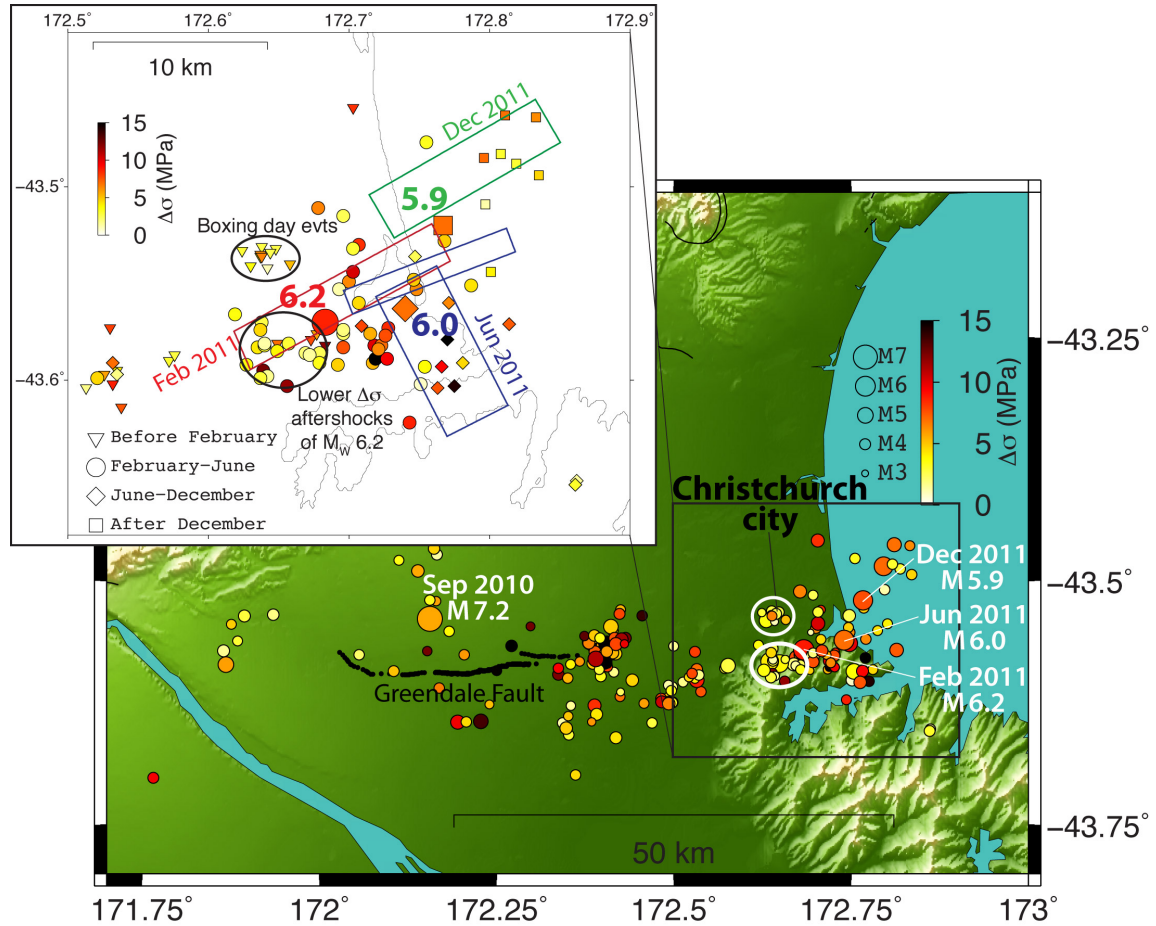
Figure 10: Lateral stress drop variations during the 2010-2011 Canterbury sequence (see also Figure 1 for event locations). Dotted black lines in the center indicate the location of the Greendale fault. Note that high stress drop events tend to cluster at the eastern edge of the Greendale fault and east of the 2011 February (M_W 6.2) hypocenter. The two white ellipses highlight two clusters of comparatively low stress drops, which are the cluster of the Boxing day events (northern ellipse, see inset and text) and the aftershocks of the M_W 6.2 Christchurch events located southwest of the event's epicenter. Inset: close-up of the Christchurch area, with fault rupture surface projections as estimated from geodetic inversion (Beavan et al., 2012). The two black ellipses correspond to the white ones in the main figure. Red rectangle represents 2011 February (M_W 6.2), blue the 2011 June (M_W 6.0) and green the 2011 December (M_W 5.9) event. The epicenters of these three events are

denoted by a larger symbol than the remaining events. Note that the fault geometries of the June and December events are not very well constrained. Events are represented by different symbols depending on their occurrence time (legend of inset).